Design and Optimization of a Novel Double-Layer Helmholtz Coil for Wirelessly Powering a Capsule Robot

Jinyang Gao, Siyu Tian, Changshun Yuan, Ziyu Ma, Chen Gao, Guozheng Yan, Ruiqin Li, Qiulin Tan, *Senior Member, IEEE*, and Li Zhang, *Fellow, IEEE*

***Abstract*—Inductively coupled wireless power transfer (IWPT) is promising to power a freely moving capsule robot (CR) continuously. The existing IWPT system for this application normally adopts a single-layer Helmholtz coil (SHC), which can generate a uniform alternating magnetic field (AMF) to cover the CR workspace but leads to low power transfer efficiency (PTE). To improve the PTE, this article proposes a novel double-layer Helmholtz coil (DHC). The DHC is composed of two in-parallel connected SHCs that have identical coil turns and winding directions but different diameters. To design and optimize the DHC, a dedicated analytical model is built and verified. A comparison between the DHC and SHC is also conducted, which shows that the DHC can not only generate a uniform AMF to cover a larger region, but its power consumption is lower when the generated AMF is identical, thus improving the PTE. Finally, the DHC is used to power a 3-D receiving coil, and the achieved PTE is in a range of 7.58%–17.41%, higher than that when using the SHC, which is in a range of 6.74%–14.92%.**

Manuscript received 29 June 2023; revised 25 August 2023; accepted 29 September 2023. Date of publication 4 October 2023; date of current version 6 December 2023. This work was supported in part by the National Natural Science Foundation of China under Grants 52275038 and 61803347, in part by Shanxi Province Science Foundation for Excellent Youth under Grant 202203021224007, in part by Key Research and Development Plan of Shanxi Province of China under Grants 201903D321164 and 2022ZDYF082, in part by the Opening Foundation of Shanxi Key Laboratory of Advanced Manufacturing Technology under Contact XJZZ202101. Recommended for publication by Associate Editor J. I. Itoh. *(Corresponding authors: Jinyang Gao; Qiulin Tan.)*

Jinyang Gao is with the State Key Laboratory of Dynamic Measurement Technology, North University of China, Taiyuan 030051, China, also with the Key Laboratory of Micro/Nano Devices and Systems, Ministry of Education, North University of China, Taiyuan 030051, China, and also with The Chinese University of Hong Kong, Hong Kong (e-mail: gjy.1001@163.com).

Siyu Tian, Ziyu Ma, Chen Gao, and Qiulin Tan are with the State Key Laboratory of Dynamic Measurement Technology, North University of China, Taiyuan 030051, China, and also with the Key Laboratory of Micro/Nano Devices and Systems, Ministry of Education, North University of China, Taiyuan 030051, China (e-mail: 1738304956@qq.com; 595229802@qq.com; s2006109@st.nuc.edu.cn; tanqiulin.99@163.com).

Changshun Yuan is with the Hangzhou Innovation Institute, Beihang University, Hangzhou 310051, China (e-mail: yuanchang61@buaa.edu.cn).

Guozheng Yan is with the School of Sensing Science and Engineering, Shanghai Jiaotong University, Shanghai 200240, China (e-mail: gzhyan@sjtu.edu.cn).

Ruiqin Li is with the Shanxi Key Laboratory of Advanced Manufacturing Technology, North University of China, Taiyuan 030051, China (e-mail: liruiqin@nuc.edu.cn).

Li Zhang is with the Department of Mechanical and Automation Engineering, The Chinese University of Hong Kong, Hong Kong (e-mail: lizhang@mae.cuhk.edu.hk).

Color versions of one or more figures in this article are available at https://doi.org/10.1109/TPEL.2023.3321845.

Digital Object Identifier 10.1109/TPEL.2023.3321845

***Index Terms*—Capsule robot (CR), double-layer Helmholtz coil (DHC), inductively coupled wireless power transfer (ICWPT), power transfer efficiency (PTE), uniform alternating magnetic field (AMF).**

I. Introduction

A CAPSULE robot (CR) that integrates an active locomotion unit and some functional modules (e.g., biopsy forceps, drug release mechanism) is promising to enable a minimally invasive diagnosis and treatment for intestinal diseases [1], [2]. However, the power demand of the multifunctional CR is up to hundreds of milliwatts [3], [4], making the power supply for it being a challenging issue, because a button battery is not sufficient to power it for a long duration and a power cable can cause a friction resistance to its locomotion. Inductively coupled wireless power transfer (IWPT) provides a promising solution to this issue, and it is implemented with a 1-D transmitting coil (1DTC) around the human abdomen and a 3-D receiving coil (3DRC) onboard the CR [5], [6]. The 1DTC normally adopts a traditional Helmholtz coil to generate a uniform and unidirectional alternating magnetic field (AMF) to cover the abdominal region and the uniform AMF is for ensuring that the CR at different locations can receive stable power. The 3DRC is constructed with three mutually orthogonal coils so that it can always induce the unidirectional AMF when the CR posture changes randomly. Because the size of the 1DTC ($\geq$400 mm) is much larger than that of the 3DRC ($\leq$15 mm), the coupling between them is very weak, thus leading to a low power transfer efficiency (PTE). To improve the PTE of the IWPT system, a lot of valuable works have been conducted in the literature.

In the 1DTC-related aspects: a class-E power amplifier is designed to drive the 1DTC, and by optimizing the circuit parameters, the efficiency of the amplifier can reach a maximum of 99.3% [7]. A self-tuning LCC inverter is proposed to drive the 1DTC whose inductance/capacitance is sensitive to the surroundings, thus avoiding excessive power loss caused by detuning and improving the PTE equivalently [8]. An analytical model for optimizing the design parameters of the traditional Helmholtz coil is built in [9], which indicates that increasing the coil turns is beneficial to improving the PTE. A noteworthy work concerning optimizing the coil structure of the 1DTC was conducted in [10] and [11], the traditional Helmholtz coil that

has two subcoils was modified to have three and four subcoils, and the modified structure was proven to improve the AMF uniformity and power transfer stability. Note that the current in the subcoils should flow in the same direction, which is beneficial to gather the AMF inside the 1DTC, thus improving the PTE to the 3DRC. If the current flows in opposite direction, typically as a cylindrical transmitting coil consisting of two subcoils for 2-D omnidirectional wireless power transfer [12], the generated AMF will mainly radiate to the surroundings, which can be used for recharging the electronic products adjacent to the transmitting coil.

In the 3DRC-related aspects, a ferrite core having the shape of a cylinder [13], cross [14], or ring [15] was inserted within the 3DRC to enhance its mutual inductance with the 1DTC, thus improving the PTE. A 2-3DRC (one 3DRC is the receiving coil, and the other is the load coil) was proposed to form a three-coil inductive link with the 1DTC, which allowed the receiving coil to have a higher quality factor for compensating the weak coupling and consequently improving the PTE [11]. An impedance-matching network constructed with two capacitors was designed to achieve the optimal load, thus maximizing the power delivered to the load and increasing the PTE with a factor of 1.73 [16]. A power management module containing a power buffer was designed to deal with the issue that the CR power demand changes with its performed functions, which can store the excessive power when the power demand is low and release it when the power demand is high, thus improving the PTE equivalently [17].

Despite the achievements mentioned above, the existing IWPT systems all use a single-layer Helmholtz coil (SHC) as the 1DTC. To further improve the PTE on the basis of existing works, this article proposes a novel double-layer Helmholtz coil (DHC), which is constructed with two in-parallel connected SHCs that have identical coil turns and winding directions but different diameters. Besides the novel coil structure of the DHC, this article contributes in the following aspects.

1) An analytical model for correlating the equivalent resistance of the DHC with its design parameters is built and verified to be correct.
2) A flow for optimizing the DHC design parameters to minimize its transmitting power when generating an AMF with the required amplitude is proposed.
3) A comparison to the SHC in terms of AMF distribution and safety, AMF uniformity, and transmitting power, is conducted to confirm the superiority of the DHC.
4) The DHC is used to power a 3DRC to validate its usefulness in improving the PTE compared to the SHC.

II. Design Overview of IWPT System and DHC

Fig. 1 presents the equivalent circuit model of the IWPT system. The transmitting side contains a signal generator for outputting a square-wave pulse signal, a voltage source for supplying a dc voltage V_{DC}, a coil driver for converting V_{DC} to an ac driving voltage V_{T} under the control of the pulse signal, a 1DTC that is represented with a lumped parameter model (L_{t}, C_{t}, R_{t}), and an inductor L_{T} and a capacitor C_{T} for tuning

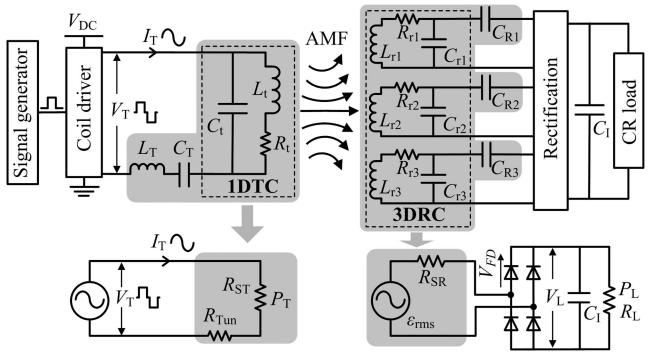

Fig. 1. Equivalent circuit model of the IWPT system.

the 1DTC. The receiving side contains a 3DRC that is also represented by a lumped parameter model, three capacitors for tuning the 3DRC, a rectification module, an integration capacitor C_{I} for voltage stabilization, and an equivalent CR load.

When the transmitting side is tuned to resonance, the 1DTC can be equivalent to a resistance R_{ST}, L_{T} and C_{T} can be equivalent to a resistance R_{Tun}, and the coil driver can be equivalent to a power source that can supply a sinusoidal driving current I_{T}. Note that the amplitude and frequency of the AMF generated by the 1DTC is controlled by I_{T}. When the receiving side is tuned to resonance, the 3DRC and tuning capacitors can be equivalent to a power source having a voltage $\varepsilon_{\mathrm{rms}}$ and an internal resistance R_{SR}, and the CR load can be equivalent to a load resistance R_{L}. Under the above equivalence, the PTE of the IWPT system can be written as

$$\eta = P_{\mathrm{L}}/P_{\mathrm{T}} \tag{1}$$

$$P_{\mathrm{L}} = V_{\mathrm{L}}^2/R_{\mathrm{L}} = \left(\frac{2\sqrt{2}\pi\varepsilon_{\mathrm{rms}}R_{\mathrm{L}} - 16V_{\mathrm{FD}}R_{\mathrm{L}}}{8R_{\mathrm{L}} + \pi^2 R_{\mathrm{SR}}}\right)^2 /R_{\mathrm{L}} \tag{2}$$

$$P_{\mathrm{T}} = \frac{1}{2}|I_{\mathrm{T}}|^2(R_{\mathrm{ST}} + R_{\mathrm{Tun}}) \approx \frac{8}{\pi^2}\frac{|V_{\mathrm{T}}|^2}{(R_{\mathrm{ST}} + R_{\mathrm{Tun}})} \tag{3}$$

where P_{L} is the load power, P_{T} is the transmitting power, V_{L} is the load voltage, and V_{FD} is the forward voltage of the diode in the rectifier. The expression of V_{L} is referenced from [17], and it is related to $\varepsilon_{\mathrm{rms}}$, R_{L}, V_{FD}, and R_{SR}. "$\approx$" in (3) is related to the relationship between $|I_{\mathrm{T}}|$ and $|V_{\mathrm{T}}|$, and it has $|I_{\mathrm{T}}| \approx [|V_{\mathrm{T}}|/(R_{\mathrm{ST}} + R_{\mathrm{Tun}})] \times (4/\pi)$, where $4/\pi$ is the Fourier coefficient because I_{T} is generated by the Fourier fundamental frequency component of V_{T} that is approximate to a square wave. The aim of this study is to improve the PTE η by using a novel DHC, and the DHC with optimized design parameters, can have a smaller R_{ST} and consequently a lower P_{T} than the SHC, when the AMFs generated by the DHC and SHC are identical.

Fig. 2 presents the design details of the DHC. The DHC is constructed with an inner-layer SHC (ISHC) and an outer-layer SHC (OSHC) that are connected in parallel, and their lead-out ends are twisted together to avoid electromagnetic interference with surroundings. The ISHC and OSHC have identical coil turns and winding directions, and an electrical insulation layer is set between them to ensure they are in coaxial. The DHC design

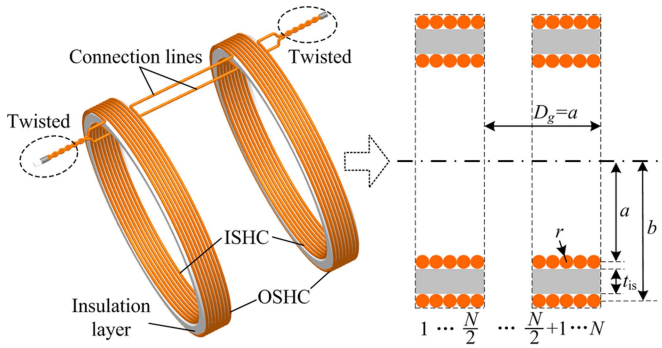

Fig. 2. Design details of the DHC.

TABLE I
DEFINITIONS OF DESIGN PARAMETERS OF DHC

Parameters		Definition
a		Radius of the ISHC, fixed as 20 cm
b		Radius of the OSHC, $b = a + 2r + t_{is}$
D_g		Distance between two sub coils, $D_g = a$
t_{is}		Thickness of the insulation layer, to be optimized
N		Coil turns of DHC/ISHC/OSHC, to be optimized
Litz wire bundle	r	Radius of litz wire bundle, r =1 mm
	r_0	Radius of litz wire bundle excluding coating, r_0 =0.99 mm
	ς	Thickness of a coating, ς =0.01 mm
	r_s	Radius of single strand in the bundle, r_s =0.051 mm
	n_s	Number of twisted strands in the bundle, n_s =180
	q	Spiral pitch of the twisted strands, q =16 mm

parameters labeled in Fig. 2 are all defined in Table I. Note that in this study, the radius of the ISHC is fixed as $a = 20$ cm to ensure an adult can lie down within it, and the distance between two subcoils D_g is set to be equal to a with the consideration of AMF uniformity. In addition, the winding wire uniformly uses a litz wire bundle having specifications listed in Table I to minimize the skin-effect loss. Thus, the DHC design parameters required to be optimized include only the coil turns N and the insulation layer thickness t_{is}.

III. Analytical Model of DHC

The analytical model of the DHC is built to correlate its equivalent resistance R_{ST} with the design parameters. By representing the DHC also with the lumped parameter model in Fig. 1, R_{ST} can be written as

$$R_{ST} = \frac{R_t}{\left(1 - 4\pi^2 f^2 L_t C_t\right)^2 + \left(2\pi f C_t R_t\right)^2} \tag{4}$$

where f is the transfer frequency. The following presents the analytical models of the inductance L_t, parasitic capacitance C_t, and ac resistance R_t of the DHC.

A. Model of Inductance

Because the ISHC and OSHC are connected in parallel and are wound in the same direction, the inductance of the DHC can be approximately calculated as [18]

$$L_t = (L_a L_b - M_{ab}^2)/(L_a + L_b - 2M_{ab}). \tag{5}$$

where L_a is the inductance of ISHC, L_b is the inductance of OSHC, and M_{ab} is the mutual inductance between ISHC and OSHC. They can be calculated as follows:

$$L_a = \sum_{i=1}^{N} L(a, r) + \sum_{i=1}^{N}\sum_{j=1}^{N} M(a_i, a_j, \rho_{ij} = 0, d_{ij})(1 - \delta_{ij}) \tag{6a}$$

$$L_b = \sum_{i=1}^{N} L(b, r) + \sum_{i=1}^{N}\sum_{j=1}^{N} M(b_i, b_j, \rho_{ij} = 0, d_{ij})(1 - \delta_{ij}) \tag{6b}$$

$$M_{ab} = \sum_{i=1}^{N}\sum_{j=1}^{N} M(a_i, b_j, \rho_{ij} = 0, d_{ij}) \tag{6c}$$

where i and j denote ith and jth turns, respectively, and it has $a_i = a_j = a$ and $b_i = b_j = b$. ρ_{ij} and d_{ij} are the lateral misalignment and axial distance between the ith and jth turns, respectively. $\delta_{ij} = 1$ when $i = j$ and $\delta_{ij} = 0$, otherwise. The concrete formulas of the self-inductance function $L(\cdots)$ and mutual-inductance function $M(\cdots)$ are given in [19]. Fig. 3 shows the calculated and measured L_t of the DHC when the design parameters are: a= 20 cm, t_{is} ∈[0, 8 cm], and N= 30, 40, and 50. Here, L_t is measured with an LCR meter (HIOKI IM3536) at a low frequency of 4 Hz. The good agreement verifies the correctness of (5) for calculating L_t of DHC.

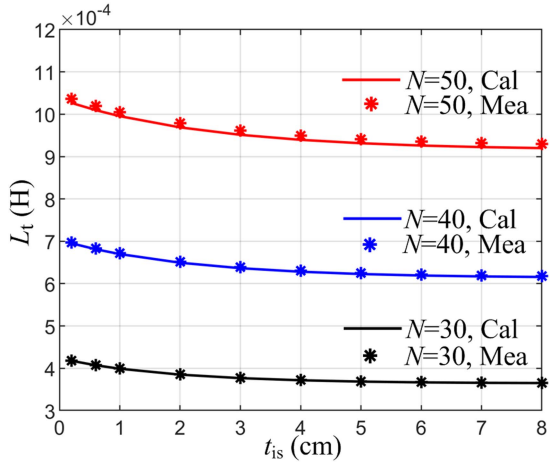

Fig. 3. Comparison of calculated and measured inductance of DHC with different design parameters.

B. Model of Parasitic Capacitance

For ISHC and OSHC that both have two subcoils, their parasitic capacitances can be respectively calculated as

$$C_a = C|_{R=a} \times (N - 2)/N^2 \tag{7a}$$

$$C_b = C|_{R=b} \times (N - 2)/N^2 \tag{7b}$$

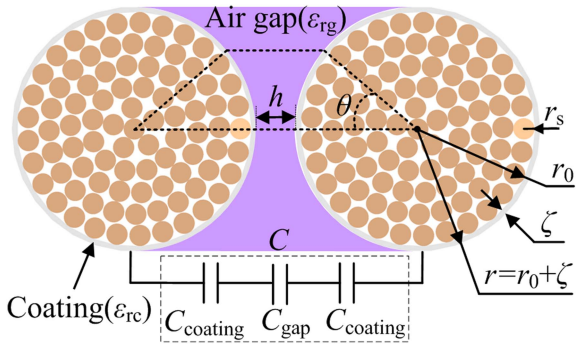

Fig. 4. Model of the parasitic capacitance between two nearby turns.

where C is the parasitic capacitance between two nearby turns of SHC, and R is the radius of SHC. C can be calculated as [20]

$$C = C_{\text{coating}} C_{\text{gap}} / (C_{\text{coating}} + 2C_{\text{gap}}) \tag{8a}$$

$$C_{\text{coating}} = 2\pi R \varepsilon_0 \varepsilon_{\text{rc}} / \ln[r/(r-\varsigma)] \tag{8b}$$

$$C_{\text{gap}} = 2\pi R \varepsilon_0 \varepsilon_{\text{rg}} / [2(1-\cos\theta) + h/r] \tag{8c}$$

where C_{cotaing} is the capacitance of the insulating coating of the litz wire bundle, and C_{gap} is the capacitance of air gap, as shown in Fig. 4. ε_0 is permittivity of vacuum, $\varepsilon_{\text{rc}}(=3)$ is relative permittivity of coating, ε_{rg} is relative permittivity of air gap and it is fitted as 1.202 by matching the measurements, $\theta(=45°)$ is facing angle of two nearby turns, and h is width of air gap and it is equal to 0 mm for a tightly wound coil. Because ISHC and OSHC are connected in parallel, the voltage difference between the same turns in them is almost equal to 0, then the parasitic capacitance between ISHC and OSHC can be neglected and the total parasitic capacitance of DHC can be calculated as

$$C_{\text{t}} = C_{\text{a}} + C_{\text{b}}. \tag{9}$$

However, C_{t}calculated with (9) cannot fit well to the measurements, especially when $t_{\text{is}} \le 3$ cm. For this reason, a more accurate calculation formula for C_{t} is used here

$$C_{\text{t}} = C_{\text{a}} p(t_{\text{is}})$$

$$p(t_{\text{is}}) = -0.0022 t_{\text{is}}^2 + 0.1116 t_{\text{is}} + 1.7509 \tag{10}$$

where $p(t_{\text{is}})$ is the fitting polynomial, and it is obtained by comparing the measured C_{t} with C_{a} calculated by (7a). Here, the measured C_{t} is obtained with $C_{\text{t}}=1/(4\pi^2 f_{\text{self}}^2 L_{\text{t}})$, where f_{self}(self-resonance frequency) and L_{t} both can be measured with the LCR meter (HIOKI IM3536). Fig. 5 presents C_{t} calculated with (10) when $a = 20$ cm, $t_{\text{is}} \in$[0, 8 cm], and N= 30, 40, and 50, which fits well with the measurements.

C. Model of AC Resistance

When I_{T} flows in the DHC, each coil turn of the DHC will be subjected to the AMF generated by the current flowing in itself and in other coil turns. The AMF can change the uniformity of the current distribution in the coil turn and cause a power loss. This power loss is directly related to the ac resistance R_{t}, and it

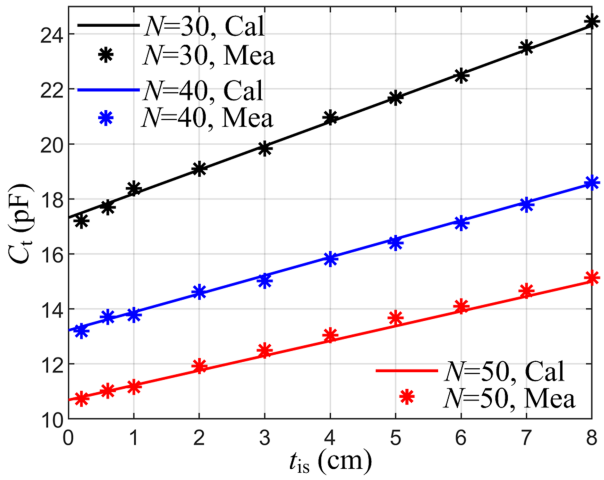

Fig. 5. Comparison of calculated and measured parasitic capacitance of DHC with different design parameters.

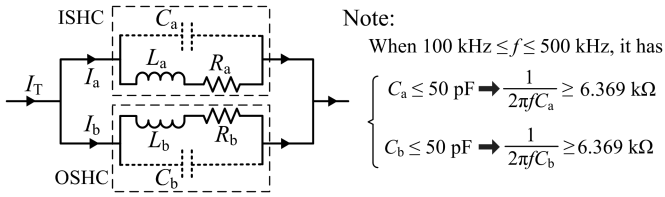

Fig. 6. Equivalent lumped parameters models of ISHC and OSHC.

is contributed by three parts

$$R_{\text{t}} = 2P_{\text{DHC}} / |I_{\text{T}}|^2 \tag{11}$$

$$P_{\text{DHC}} = P_{\text{s}} + P_{\text{p\_int}} + P_{\text{p\_ext}} \tag{12}$$

where P_{DHC} is the total power loss of the DHC. P_{s} is the power loss caused by the skin effect of each strand in the litz wire bundle, and it is related to the AMF generated by the current flowing in the strand itself. $P_{\text{p\_int}}$ and $P_{\text{p\_ext}}$ are the power losses caused by internal and external proximity effects, and they are related to an internal AMF $\mathbf{H_{int}}$ and an external AMF $\mathbf{H_{ext}}$ that are exerted at each strand, respectively.

1) Current Division in ISHC and OSHC: To analyze the AMF generated by the DHC, the current division in ISHC and OSHC, is required to be determined first. For this aim, ISHC and OSHC are both represented with the lumped parameter model shown in Fig. 6. As calculated in the previous section, the parasitic capacitance $C_{\text{a}}(C_{\text{b}})$ is normally less than 50 pF, thus when the transfer frequency is in a commonly used range of 100–500 kHz [3], [4], [5], [9], [10], [11], the capacitive reactance is in the order of kilohm, much larger than the ac resistance $R_{\text{a}}(R_{\text{b}})$ that is normally less than 10 Ω. Therefore, the parasitic capacitance branch can be considered open circuit. Then, by abiding the rule that the terminal voltages of ISHC and OSHC are equal to each other, it has

$$I_{\text{a}} R_{\text{a}} + L_{\text{a}} \frac{dI_{\text{a}}}{dt} + M_{\text{ab}} \frac{dI_{\text{b}}}{dt} = I_{\text{b}} R_{\text{b}} + L_{\text{b}} \frac{dI_{\text{b}}}{dt} + M_{\text{ab}} \frac{dI_{\text{a}}}{dt} \tag{13}$$

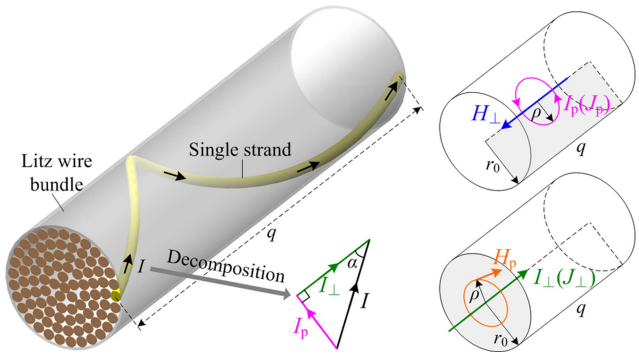

Fig. 7. 3-D view of the litz wire bundle, and the generated AMF when a sinusoidal AC current I flows into it.

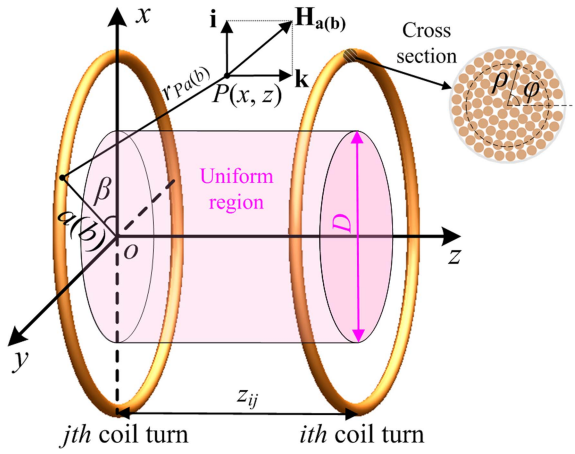

Fig. 8. AMF generated by the jth coil turn in the xoz plane.

where L_a, L_b, and M_ab can be calculated with (6). When the DHC is in resonance, I_a and I_b are in the same phase and both have a sinusoidal form

$$I_{\mathrm{a(b)}} = |I_{\mathrm{a(b)}}| \sin(2\pi f t). \tag{14}$$

By substituting (14) into (13), the division ratio can be approximately derived as

$$|I_\mathrm{a}|/|I_\mathrm{b}| \approx (L_\mathrm{b} - M_\mathrm{ab})/(L_\mathrm{a} - M_\mathrm{ab}). \tag{15}$$

2) Calculation of AMF $\mathbf{H_{int}}$ *and* $\mathbf{H_{ext}}$*:* The internal AMF $\mathbf{H_{int}}$ exerted at each strand is generated by the current flowing in other strands in the same litz wire bundle. Because each strand carrying the current spirals forward, the current I flowing into the litz wire bundle can be considered to have two components of I_p and $I_\perp$, as shown in Fig. 7. I_p is in the cross section of the litz wire bundle and it generates $H_\perp$ that is perpendicular to the cross section, whereas $I_\perp$ is perpendicular to the cross section and it generates H_p that is in the cross section. By referring to the magnetic field formula of infinite solenoid and Ampere law, $\mathbf{H_{int}}$ at polar radius ρ can be derived as

$$\mathbf{H_{int}}(\rho) = H_\perp(\rho) \cdot \mathbf{u} + H_\mathrm{p}(\rho) \cdot \mathbf{v} \tag{16a}$$

$$H_\perp(\rho) = I(r_0 - \rho)\sin\alpha\tan\alpha/(2\pi r_0^2) \tag{16b}$$

$$H_\mathrm{p}(\rho) = I\rho\cos\alpha/(2\pi r_0^2) \tag{16c}$$

where $\mathbf{u}$ is the unit vector perpendicular to the cross section,$\mathbf{v}$ is the unit vector that is tangent to the circle with a radius ρ in the cross section, α is spiral slant angle, and it has $\alpha = \arctan(2\pi r_0/q)$.

The external AMF $\mathbf{H_{ext}}$ exerted at each strand is generated by the current flowing in other coil turns in the DHC. Here, $\mathbf{H_{ext\_ai}}$ and $\mathbf{H_{ext\_bi}}$ are used to specifically denote the external AMF at the ith coil turn of ISHC and OSHC, respectively, and they can be calculated as

$$\mathbf{H_{ext}} \begin{cases} \mathbf{H_{ext\_ai}} = \mathbf{H_{a\_ai}} + \mathbf{H_{b\_ai}} \\ \mathbf{H_{ext\_bi}} = \mathbf{H_{a\_bi}} + \mathbf{H_{b\_bi}} \end{cases} \tag{17}$$

where $\mathbf{H_{a\_ai}}$ and $\mathbf{H_{b\_ai}}$ are the AMF at ith coil turn of ISHC that are generated by other coil turns of ISHC and OSHC, respectively, and $\mathbf{H_{a\_bi}}$ and $\mathbf{H_{b\_bi}}$ are the AMF at the ith coil turn of OSHC that are generated by other coil turns of ISHC and OSHC, respectively. Because of the circular symmetry of ISHC and OSHC, the AMF generated by each coil turn in the xoz plane can represent the AMF in 3-D space, as shown in Fig. 8. Using a polar radius ρ and a polar angle φ to denote any point in the cross section of the litz wire bundle, where $\mathbf{H_{a\_ai}}$, $\mathbf{H_{b\_ai}}$, $\mathbf{H_{a\_bi}}$, and $\mathbf{H_{b\_bi}}$ can be calculated as

$$\mathbf{H_{a\_ai}}(\rho,\varphi) = \sum_{j=1,j\neq i}^{N} \mathbf{H_a}(a + \rho\sin\varphi, z_{ij} + \rho\cos\varphi) \tag{18a}$$

$$\mathbf{H_{b\_ai}}(\rho,\varphi) = \sum_{j=1}^{N} \mathbf{H_b}(a + \rho\sin\varphi, z_{ij} + \rho\cos\varphi) \tag{18b}$$

$$\mathbf{H_{a\_bi}}(\rho,\varphi) = \sum_{j=1}^{N} \mathbf{H_a}(b + \rho\sin\varphi, z_{ij} + \rho\cos\varphi) \tag{18c}$$

$$\mathbf{H_{b\_bi}}(\rho,\varphi) = \sum_{j=1,j\neq i}^{N} \mathbf{H_b}(b + \rho\sin\varphi, z_{ij} + \rho\cos\varphi) \tag{18d}$$

where z_{ij} is the distance between the jth and ith coil turns in the oz direction, and $\mathbf{H_a}$ and $\mathbf{H_b}$ are the AMF generated by the jth coil turn of ISHC and OSHC, respectively. Note that the two items in the brackets of $\mathbf{H_a}$ and $\mathbf{H_b}$ denote x and z coordinates of the point (ρ,φ) relative to the origin O, and O is set at the center of the jth coil turn. Referring to Biot–Savart's law, $\mathbf{H_a}$ and $\mathbf{H_b}$ at an arbitrary point $P(x,z)$ can be derived as

$$\mathbf{H_a}(x,z) = \frac{aI_a}{4\pi}\int_0^{2\pi} \frac{z\cos\beta\cdot\mathbf{i} + (a - x\cos\beta)\cdot\mathbf{k}}{r_{Pa}^3(x,z)} d\beta \tag{19a}$$

$$\mathbf{H_b}(x,z) = \frac{bI_b}{4\pi}\int_0^{2\pi} \frac{z\cos\beta\cdot\mathbf{i} + (b - x\cos\beta)\cdot\mathbf{k}}{r_{Pb}^3(x,z)} d\beta \tag{19b}$$

where $\mathbf{i}$ and $\mathbf{k}$ are unit vectors along ox and oz directions, respectively, and r_{Pa} and r_{Pb} are the distances between the point $P(x,z)$ and the jth coil turns of ISHC and OSHC, respectively.

3) Power Loss Caused by Skin Effect: Assuming the current flowing in a litz wire bundle is uniformly distributed in each strand, then the skin effect caused power loss is calculated as

$$P_{\mathrm{s}} = P_{\mathrm{s\_a}} + P_{\mathrm{s\_b}} \tag{20a}$$

$$P_{\mathrm{s\_a}} = n_{\mathrm{s}} R_{\mathrm{ac\_u}} (2\pi a N/\cos\alpha)(|I_{\mathrm{a}}|/\sqrt{2}n_{\mathrm{s}})^2 \tag{20b}$$

$$P_{\mathrm{s\_b}} = n_{\mathrm{s}} R_{\mathrm{ac\_u}} (2\pi b N/\cos\alpha)(|I_{\mathrm{b}}|/\sqrt{2}n_{\mathrm{s}})^2 \tag{20c}$$

$$R_{\mathrm{ac\_u}} = \frac{\gamma_{\mathrm{s}}}{2\sigma\pi r_{\mathrm{s}}^2} \frac{\mathrm{ber}(\gamma_{\mathrm{s}})\mathrm{bei}'(\gamma_{\mathrm{s}}) - \mathrm{bei}(\gamma_{\mathrm{s}})\mathrm{ber}'(\gamma_{\mathrm{s}})}{\mathrm{ber}'^2(\gamma_{\mathrm{s}}) + \mathrm{bei}'^2(\gamma_{\mathrm{s}})} \tag{20d}$$

where $P_{\mathrm{s\_a}}$ and $P_{\mathrm{s\_b}}$ are the skin effect caused power losses of ISHC and OSHC, respectively, $R_{\mathrm{ac\_u}}$ is skin-effect related resistance of single strand per unit length [21], $\gamma_{\mathrm{s}} = \sqrt{2}r_{\mathrm{s}}/\delta$, where δ is the skin depth ($=1/\sqrt{\pi\mu_0\mu_{\mathrm{r}}\sigma f}$, where μ_0 is air permeability, μ_{r} is relative permeability, and σ is conductivity of copper), ber() and bei() are the real and imaginary parts of zeroth-order Kelvin functions, respectively, and ber′() and bei′() are the first derivatives of ber() and bei(), respectively. Note that the item $\cos\alpha$ in (20b) and (20c) is for considering the length increment caused by twisting the strands in the litz wire bundle.

4) Power Loss Caused by Internal Proximity Effect: The internal proximity effect caused by power loss is calculated as

$$P_{\mathrm{p\_int}} = P_{\mathrm{p\_int\_a}} + P_{\mathrm{p\_int\_b}}, \tag{21a}$$

$$P_{\mathrm{p\_int\_a}} = n_{\mathrm{s}} P_{\mathrm{strand\_u\_a}} (2\pi a N) \tag{21b}$$

$$P_{\mathrm{p\_int\_b}} = n_{\mathrm{s}} P_{\mathrm{strand\_u\_b}} (2\pi b N) \tag{21c}$$

$$P_{\mathrm{strand\_u\_a}} = G(\gamma_{\mathrm{s}}) \frac{\int_0^{r_0} |\mathbf{H_{int}}(\rho, I = I_{\mathrm{a}})|^2 2\pi\rho d\rho}{\pi r_0^2} \tag{21d}$$

$$P_{\mathrm{strand\_u\_b}} = G(\gamma_{\mathrm{s}}) \frac{\int_0^{r_0} |\mathbf{H_{int}}(\rho, I = I_{\mathrm{b}})|^2 2\pi\rho d\rho}{\pi r_0^2} \tag{21e}$$

$$G(\gamma_{\mathrm{s}}) = \frac{-2\pi\gamma_{\mathrm{s}}}{\sigma} \cdot \frac{\mathrm{ber}_2(\gamma_{\mathrm{s}})\mathrm{ber}'(\gamma_{\mathrm{s}}) + \mathrm{bei}_2(\gamma_{\mathrm{s}})\mathrm{bei}'(\gamma_{\mathrm{s}})}{\mathrm{ber}^2(\gamma_{\mathrm{s}}) + \mathrm{bei}^2(\gamma_{\mathrm{s}})} \tag{21f}$$

where $P_{\mathrm{p\_int\_a}}$ and $P_{\mathrm{p\_int\_b}}$ are internal proximity effect caused power losses of ISHC and OSHC, respectively, $P_{\mathrm{strand\_u\_a}}$ and $P_{\mathrm{strand\_u\_b}}$ are power losses of single strand per unit length in ISHC and OSHC, respectively, $G(\gamma_{\mathrm{s}})$ is a conversion function correlating the internal AMF with power loss of single strand [21], and $\mathrm{ber}_2()$ and $\mathrm{bei}_2()$ are the real and imaginary parts of second-order Kelvin functions, respectively. Note that in (21d) and (21e), $|\mathbf{H_{int}}|^2$ is averaged over the cross section of the litz wire bundle; this is because each strand can appear at all positions of the cross section along its spiral path, thus the average of the AMF along the spiral path of each strand can be considered equal to the average over the cross section.

5) Power Loss Caused by External Proximity Effect: The external proximity effect caused power loss is calculated as

$$P_{\mathrm{p\_ext}} = P_{\mathrm{p\_ext\_a}} + P_{\mathrm{p\_ext\_b}} \tag{22a}$$

$$P_{\mathrm{p\_ext\_a}} = \sum_{i=1}^{N} n_{\mathrm{s}} \cdot 2\pi a \cdot G(\gamma_{\mathrm{s}}) \frac{\int_0^{2\pi}\int_0^{r_0} |\mathbf{H_{ext\_ai}}|^2 \rho d\rho d\varphi}{\pi r_0^2} \tag{22b}$$

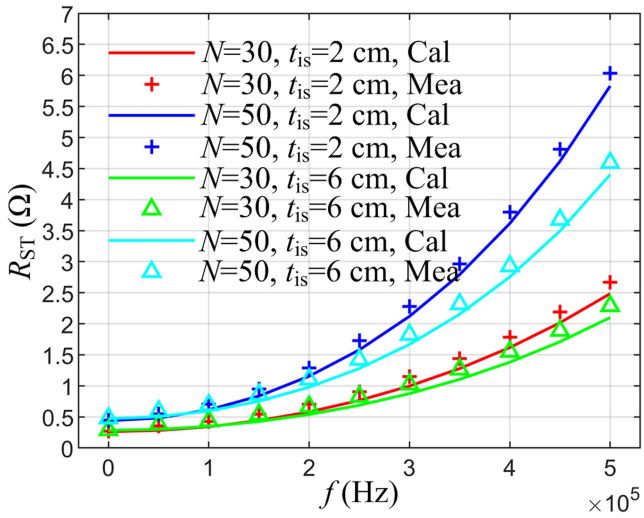

Fig. 9. Change of calculated and measured R_{ST} with frequency.

$$P_{\mathrm{p\_ext\_b}} = \sum_{i=1}^{N} n_{\mathrm{s}} \cdot 2\pi b \cdot G(\gamma_{\mathrm{s}}) \frac{\int_0^{2\pi}\int_0^{r_0} |\mathbf{H_{ext\_bi}}|^2 \rho d\rho d\varphi}{\pi r_0^2} \tag{22c}$$

where $P_{\mathrm{p\_ext\_a}}$ and $P_{\mathrm{p\_ext\_b}}$ are external proximity effect caused power losses of ISHC and OSHC, respectively. Note that in (26b) and (26c), $|\mathbf{H_{ext\_ai}}|^2$ and $|\mathbf{H_{ext\_bi}}|^2$ are also averaged over the cross section of the litz wire bundle, for a similar reason of averaging $|\mathbf{H_{int}}|^2$.

D. Model Verification

To verify the correctness of the model built above, the calculated R_{ST} is compared to the measured ones, as shown in Fig. 9. It can be found that the following statements hold.

1) The measured results are all a bit larger than the calculated ones; this may be because the power losses of the connection lines between the subcoils are not considered in the calculation. Also, the differences between the measured and calculated results increase slowly with f, which may be led by that f can amplify the calculated errors of L_{t}, C_{t}, and R_{t}, as indicated by (4). However, the difference is small and is about 0.2 Ω when f = 500 kHz, thus verifying the correctness of the built model for calculating R_{ST} of the DHC.
2) When f is relatively low, R_{ST} when t_{is}= 6 cm is a bit larger than that when t_{is}= 2 cm; with the increase of f, R_{ST} of the former becomes smaller than that of the later, manifesting that the increase of t_{is} is beneficial to reduce R_{ST} of the DHC at a high frequency.

IV. Optimization of DHC and Comparison to SHC

A. Optimization of DHC Design Parameter

As shown in Fig. 10, the optimization flow of the DHC design parameters (N and t_{is}) is designed at a certain f, and the optimization aim is to find the optimal N and t_{is} that can

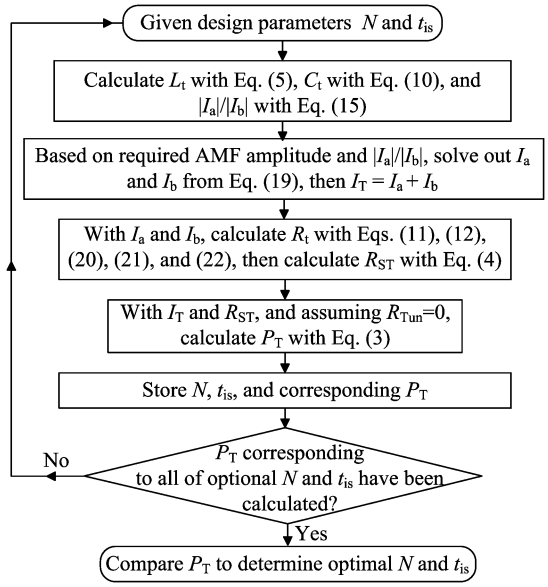

Fig. 10. Optimization flow of DHC design parameters at a certain f.

minimize P_T of DHC when generating the AMF with required amplitude. Note that for a different f, or a different ISHC radius a, or a litz wire bundle with other specifications, this flow is also applicable. Fig. 11 shows the changes of P_T, R_{ST}, and I_T with N and t_{is}, when $f=$ 300 kHz and the required AMF amplitude at DHC center is 10^{-4} T. It can be found that the following statements hold.

1) With the increase of N, P_T decreases as a whole. This is because although R_{ST} increases with N, I_T required for generating the AMF with the amplitude of 10^{-4} T decreases rapidly with N, thus resulting in a decrease of P_T ultimately.
2) With the increase of t_{is}, P_T first decreases rapidly and then increases slowly. This is because when t_{is} is small, the external AMF $\mathbf{H}_{\mathbf{b\_ai}}$ and $\mathbf{H}_{\mathbf{a\_bi}}$ are both large and can lead to a large power loss, at this time increasing t_{is} can make the external AMF decrease rapidly and consequently lower R_{ST} and P_T. With t_{is} continuing to increase, R_{ST} decreases more and more slowly and even begins to increase, and I_T required for generating the AMF with the amplitude of 10^{-4} T increases, making P_T begin to increase.

The above results manifest that P_T can be lowered by selecting a large N and a suitable t_{is}.

B. Comparison Between DHC and SHC

In the following comparison, the radius and distance between two subcoils of the SHC are set to be equal to those of the ISHC, to ensure the internal region sizes of the DHC and SHC are identical.

1) Comparison of AMF Distribution and Safety: The AMF distribution of DHC and SHC is observed with a simulation software of COMSOL Multiphysics. Fig. 12 shows the simulation results in the *xoz* plane. When the AMF amplitudes at DHC and

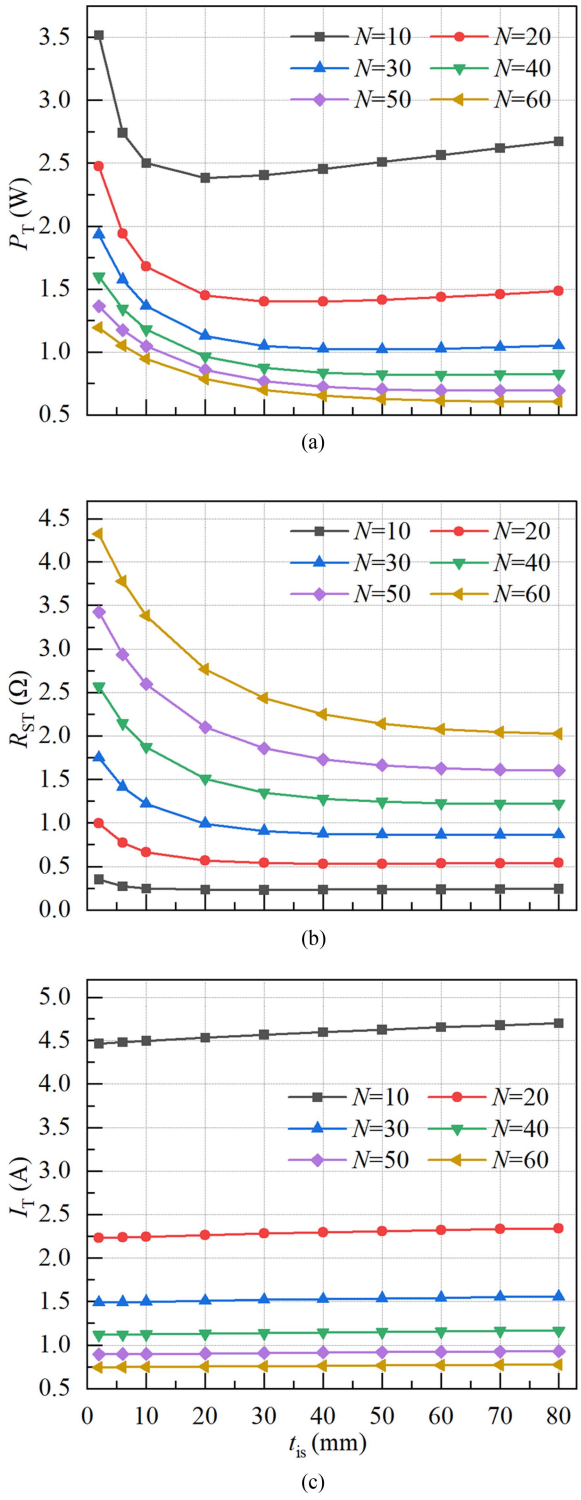

Fig. 11. Change of (a) P_T, (b) R_{ST}, and (c) I_T with N and t_{is}, when $f=$ 300 kHz and the required AMF amplitude at the DHC center is 10^{-4} T.

SHC center are both 10^{-4} T, N of DHC and SHC are both 50, and t_{is} of DHC is 40 mm. It can be found that the following statements hold.

1) DHC and SHC can both generate uniform AMF inside themselves. This is owing to that the current in the left

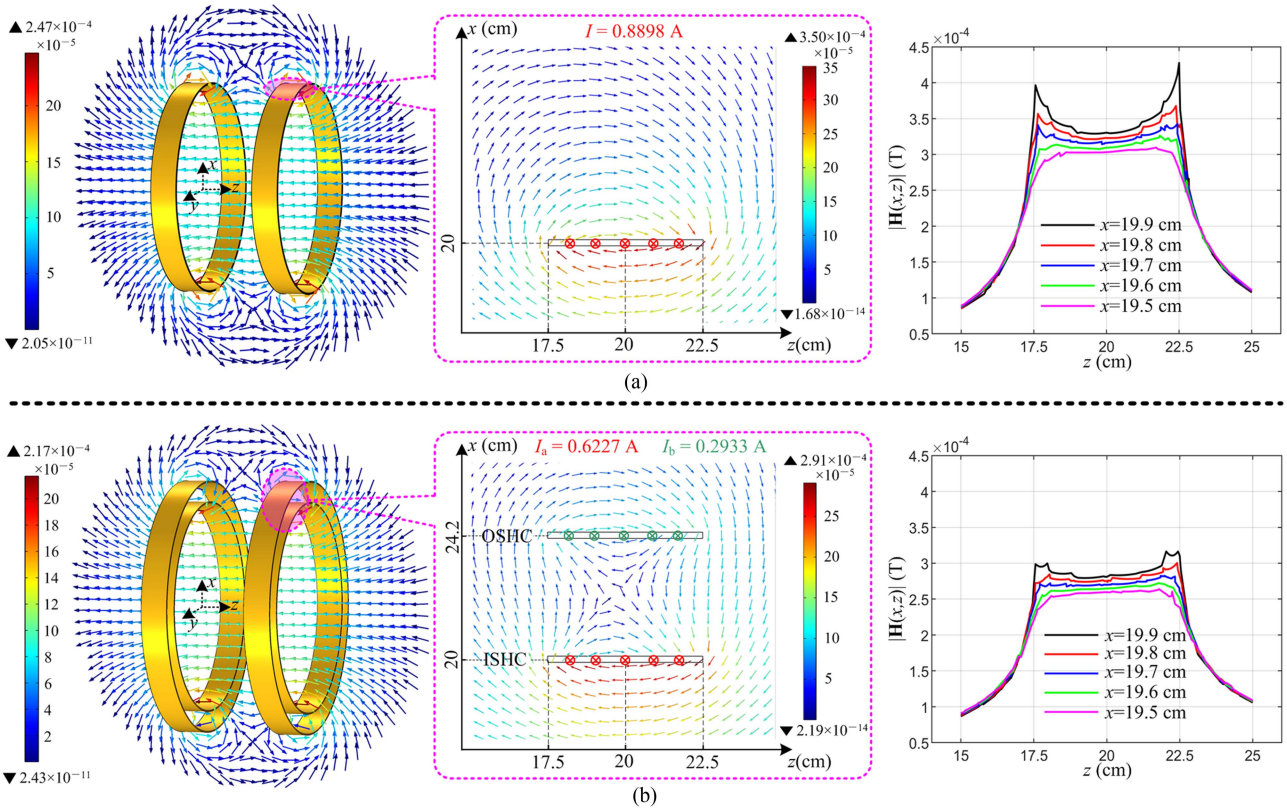

Fig. 12. AMF distribution of (a) SHC and (b) DHC. The left figures show the overall distribution of the AMF in the xoz plane. The middle figures show the AMF distribution details around the right subcoil. The right figures show the AMF amplitude near the winding wire of the right subcoil. Note that the unit of the color bar is T (Tesla).

and right subcoils flows in the same direction, making the z-axis component of the generated AMF inside the DHC/SHC have identical direction, which superposes each other to form the uniform AMF along the z-axis.

2) The AMF amplitude inside the DHC/SHC is obviously larger than that outside them. This is because the AMF inside and outside the DHC/SHC always forms a closed loop, whereas the AMF outside distributes in a much larger region, causing its amplitude to be smaller than that inside the DHC/SHC.

3) As shown in the middle of Fig. 12(b), the AMF in the rectangle region between the ISHC and OSHC basically points to four directions, i.e., up, left, down, and right, and reaches a minimum in the region center. This is because the currents in the ISHC and OSHC both flow inward on the paper surface. The z-axis component of the AMF generated by them has opposite directions and counteracts each other, and the counteracting is complete in the center. While the x-axis component has the same direction and superposes each other, which both points up in the left half region and down in the right half region.

4) The AMF amplitude reaches a peak near the winding wire. To clearly observe the difference in the AMF peak between the DHC and SHC, the AMF amplitude in the region of $x \in$[19.5 cm, 19.9 cm] and $z \in$[15 cm, 25 cm] is extracted and plotted with the curve. This region is inside and near the winding wire of the right subcoil, which has a width of 5 cm. It can be found that the closer to the winding wire, the larger the AMF amplitude. Also, the AMF peak of SHC is all obviously larger than that of DHC at each x. For example, when x =19.9 cm, the AMF peak of SHC is 4.277×10^{-4} T (z =22.5 cm), much larger than that of DHC, which is 3.164×10^{-4} T (z =22.04 cm and 22.44 cm). This is owing to that when generating identical AMF in the DHC/SHC center, the driving current of DHC (0.9160 A) is divided into ISHC (0.6227 A) and OSHC (0.2933 A), and the current in ISHC is smaller than that in SHC (0.8898 A). The above results manifest that the DHC is safer in avoiding peak electromagnetic exposure.

Note that the AMF peak of DHC/SHC has different values in Fig. 12, which is related to the grid size when taking the simulation results to plot the figure. The smaller the grid size, the larger the AMF peak.

2) Comparison of AMF Uniformity: The AMF uniformity is described with an index of divergence D_{iv} here, and the AMF is considered uniform if

$$D_{\text{iv}}(x,z) = \frac{|\text{Proj}_{\mathbf{H_0}}\mathbf{H}(x,z)| - |\mathbf{H_0}|}{|\mathbf{H_0}|} \times 100\% \leq 10\% \quad (23)$$

where $\mathbf{H}(x,z)$ is the AMF at point (x,z), $\mathbf{H_0}$ is the AMF at the DHC/SHC center, and $\text{Proj}_{\mathbf{H_0}}\mathbf{H}(x,z)$ is the projection of $\mathbf{H}(x,z)$ in the direction of $\mathbf{H_0}$. With (23), (19) that can

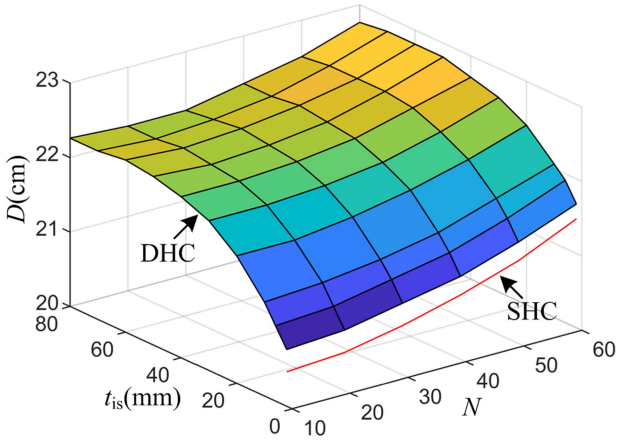

Fig. 13. Change of the AMF uniform region diameter D with the DHC/SHC design parameters N and t_{is}.

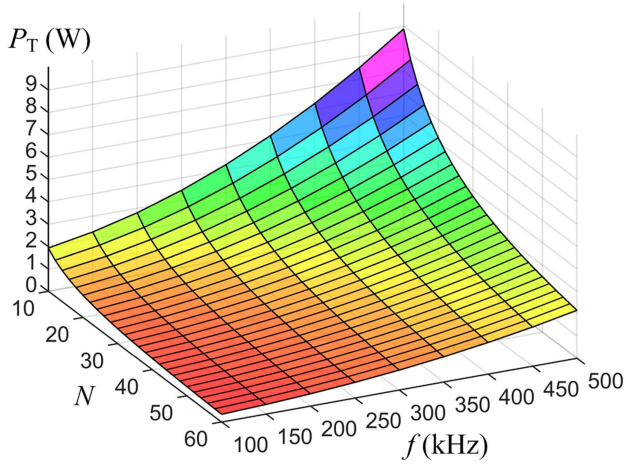

Fig. 14. Chang of P_T of SHC with N at different f.

be used for calculating $\mathbf{H}(x, z)$ and $\mathbf{H_0}$, and the simulation results shown in Fig. 12, we find that the uniform AMF basically forms a rectangle region in the xoz plane. Because the DHC and SHC are both circular symmetric, the uniform AMF can form a cylindrical region in 3-D space (refer to Fig. 8), which just fits to the cylindrical shape of the human waist and abdomen. Here, we use D to denote the uniform region diameter, and Fig. 13 shows the change of D with DHC/SHC design parameters. It can be found that D of DHC increases with N and t_{is}, and D of SHC increases with N. Also, D of DHC is always larger than that of SHC, even when t_{is} takes a minimum of 2 mm. This is because DHC is constructed with an ISHC with a radius a and an OSHC with a radius $b(>a)$, and its equivalent radius is larger than the SHC radius a. As reported in [9], the larger the coil radius, the larger the uniform AMF region.

3) Comparison of Transmitting Power P_T: In this comparison, the design parameters of DHC/SHC are selected in commonly used ranges, i.e., $N \in$[10, 60] and $t_{is} \in$[2 mm, 80 mm]. The comparison standard is the transmitting power P_T of DHC/SHC when the generated $\mathbf{H_0}$ has identical amplitude (10^{-4} T) and frequency (100–500 kHz).

Before the comparison, the influence of N on P_T of SHC is analyzed, with a flow similar to that presented in Fig. 10. Fig. 14 shows the change of P_T of SHC with N, which indicates that the optimal N is all equal to 60 for SHC at different f.

Fig. 15 shows P_T of SHC when $N = 60$, P_T of DHC when $N = 60$ and $t_{is} = 2$ mm, 10 mm, 30 mm, and the optimized values. Note that the optimized t_{is} is obtained with the flow shown in Fig. 10. It can be found that the following statements hold.

1) When $t_{is} = 2$ mm and 10 mm, P_T of DHC is first slightly lower than that of SHC, but with the increase of f, it becomes significantly higher than that of SHC. This manifests that a small t_{is} is not suitable for DHC, especially at a high f.
2) With the increase of f, the optimized t_{is} increases rapidly from 37 mm and then gradually stabilizes around 70 mm. When using the optimized t_{is}, P_T of DHC can be at least 20.18% ($f = 500$ kHz) lower than that of SHC.

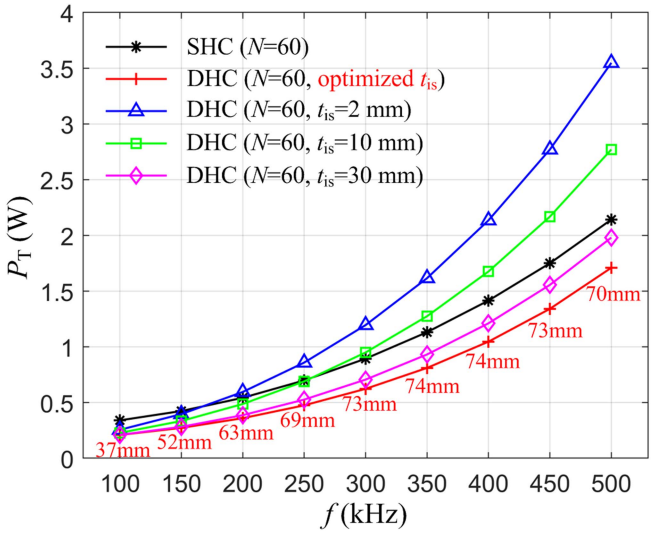

Fig. 15. Comparison of P_T of SHC and DHC when the generated $\mathbf{H_0}$ has identical amplitude (10^{-4} T) and frequency (100–500 kHz).

The above results manifest that when generating identical $\mathbf{H_0}$, P_T of DHC can be lower than that of SHC by selecting an appropriate t_{is}.

V. Experiment

A. Experimental Setup

To verify the benefit of the proposed DHC in lowering transmitting power, the experimental setups shown in Fig. 16 are constructed, which involve a driving circuit for generating an ac driving voltage, an SHC, a DHC and a 3DRC prototypes, a power management circuit for 3DRC, a load (= 30 Ω), and an oscilloscope (Tektronix DPO 2024B) for observing the ac driving voltage V_T, and the load voltage V_L.

The design parameters of the SHC, DHC, and 3DRC are listed in Tables II and III. The SHC and DHC both use the optimized design parameters (i.e., $N = 60$, $t_{is} = 70$ mm), and they are constructed by winding the litz wire bundle around

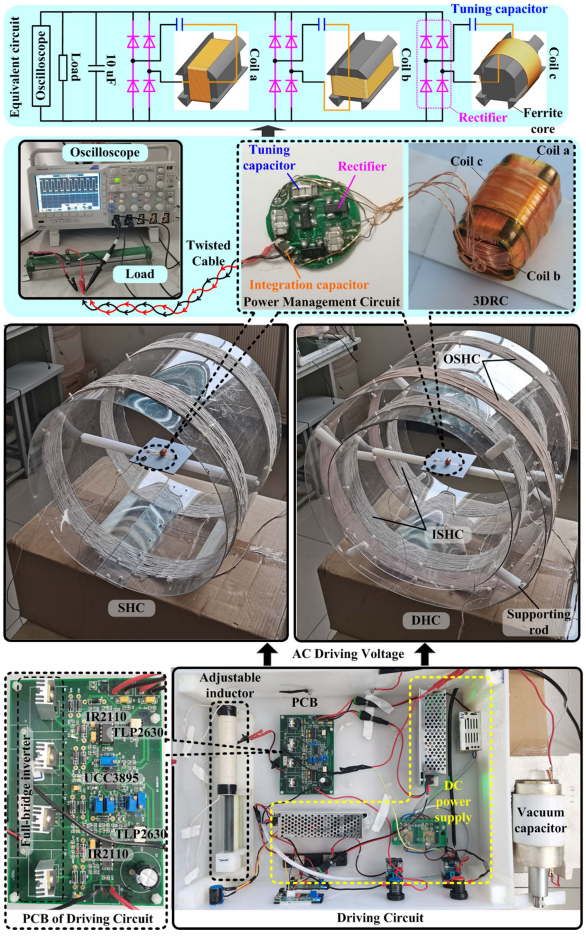

Fig. 16. Experimental setups for verifying the benefit of the DHC.

TABLE II
DESIGN PARAMETERS OF THE SHC AND DHC

Parameter	SHC	DHC
Winding wire	Litz wire bundle, with specifications listed in Table I	
Number of turns	60	60
Radius	20 cm	ISHC 20 cm OSHC 27 cm
L_t (mH)	1.4186	1.2782
C_t (pF)	5.0735	12.2143

TABLE III
DESIGN PARAMETERS OF THE 3DRC

Parameters		Coil a	Coil b	Coil c
Total size (mm)		Φ 10.6×15		
Winding wire		AWG35 enameled copper wire		
Number of turns		80	80	80
Mean size (mm)		12.45×7.45	13.35×7.45	Φ 10.3
Ferrite core(≤ 500 kHz)	Material	Manganese-Zinc Ferrite, R2K, by MMG-Neosid Ltd.		
	Size (mm)	Φ 10×15, having grooves for winding wire at lateral and end faces		
	E-factor	2.9562	2.8243	4.1577
L_t (μH)		292.453	274.455	219.650
C_t (pF)		32.440	32.864	55.368

TABLE IV
RESISTANCES OF THE SHC, DHC, AND 3DRC AT DIFFERENT FREQUENCY

f (kHz)	SHC		DHC		3DRC		
	R_{ST} (Ω)	R_{Tun} (Ω)	R_{ST} (Ω)	R_{Tun} (Ω)	R_{SR_a} (Ω)	R_{SR_b} (Ω)	R_{SR_c} (Ω)
100	1.24	0.97	0.81	0.9	5.16	5.02	4.12
150	1.57	0.99	1.04	1.21	6.64	6.31	5.05
200	2.06	1.14	1.33	1.12	8.70	8.10	6.25
250	2.63	1.4	1.78	1.42	11.33	10.37	7.77
300	3.37	1.67	2.29	1.67	14.61	13.18	9.65
350	4.32	2.15	2.94	2.13	18.65	16.63	11.97
400	5.43	2.43	3.81	2.52	23.52	20.76	14.80
450	6.74	3.21	4.83	2.81	29.30	25.72	18.25
500	8.18	3.72	6.11	3.68	36.22	31.47	22.44

the cylindrical plastic (polyvinyl chloride) shell. Note that the electrical insulation layer between the ISHC and OSHC of the DHC is just air because air is a good electrical insulator, and several plastic supporting rods having equal length are evenly set between the ISHC and OSHC to form the insulation layer and ensure the ISHC and OSHC are in coaxial.

The 3DRC is composed of three mutually orthogonal coils a, b, and c, and an inserted cylindrical ferrite core with side grooves, as shown in the upper part of Fig. 16. The coils a and b are both rectangular, and they are wound along the side grooves of the ferrite core. The coil c is circular and it is wound around the circumference of the ferrite core. The ferrite core can enhance the induced electromotive force (emf) compared to the air-core case [22], and its E (enhancement)-factor is listed in Table III, which is measured by comparing the emfs of the ferrite-core and air-core 3DRCs. Because the employed ferrite core has a frequency range of up to 500 kHz, the E-factor can remain stable when $f \leq 500$ kHz. Note that when f changes, the SHC, DHC, and 3DRC are required to be retuned by changing the tuning components, and their related resistances at different f are listed in Table IV.

The power management circuit has a diameter of 11 mm and a thickness of 1.7 mm, which integrates three sets of tuning capacitors and three full-bridge rectifiers (BAS4002A by Infineon Technologies). Its equivalent circuit is shown in the upper part of Fig. 16. The tuned coils a, b, and c are connected to three rectifiers, respectively, and then the outputs of the three rectifiers are connected in parallel. Because of the clamping effect of the diodes in the rectifier, only the coil generating the maximum ε_{rms} can output to the load at any time, and the other two coils can be considered to be open circuits. The parallel connection but not the series connection is adopted here because the CR load normally has a value less than 30 Ω when the parallel connection can enable the 3DRC to output a larger average power, which has been verified in a previous study [23]. The integration capacitor selects a value of 10 μF by experience. When being integrated into the CR, the power management circuit can be fixed at one end face of the 3DRC because they have similar diameters.

B. Experimental Results

Fig. 17 shows the measured waveforms of V_T and V_L at different f when the 3DRC was centered in the DHC/SHC

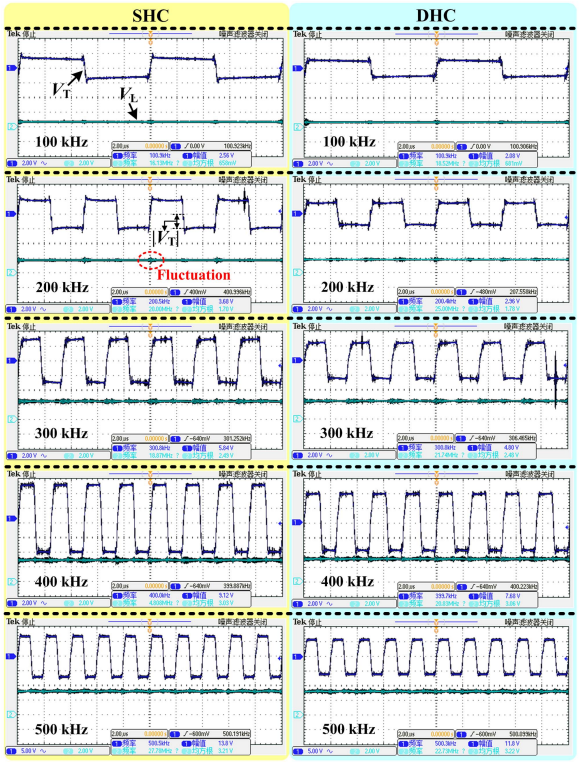

Fig. 17. Waveforms of V_T and V_L at different f when $|\mathbf{H_0}|= 10^{-4}$ T and the central axis of the coil c of the 3DRC was aligned with that of the DHC/SHC.

and the central axis of its coil c was aligned with that of the DHC/SHC. Here, $|\mathbf{H_0}|$ was fixed as 10^{-4} T and the required $|I_T|$ of the DHC and SHC was 0.77 A and 0.74 A, respectively. The waveform of V_T but not I_T was measured because the series connection of an ammeter can affect the resonance. It can be found that the following statements hold.

1) With the increase of f, $|V_T|$ for generating the fixed $|\mathbf{H_0}|$ increases. This is because although $|I_T|$ for generating the fixed $|\mathbf{H_0}|$ is certain, R_{ST} and R_{Tun} increase with f, thus causing the increase of $|V_T|$.
2) At each f, $|V_T|$ of SHC is always a bit larger than that of DHC, and V_L is basically identical to each other, manifesting $\mathbf{H_0}$ generated by the SHC and DHC is identical.
3) V_L is basically stable thanks to the integral action of the 10-μF capacitor, but also has some small fluctuations that appear more frequently with the increase of f. To eliminate the fluctuation, a voltage regulator can be used in the future.

V_T and V_L when the central axes of the coils a and b were, respectively, aligned with that of the DHC/SHC, were also measured. With the measurements and (1)–(3), the changes of $\eta_{a(b)(c)}$, P_T, and $P_{L\_a(b)(c)}$ with f can be obtained, as shown in Fig. 18. Here, the subscript a(b)(c) indicates the case that the central axis of the coil a(b)(c) is aligned with that of the DHC/SHC. It can be found that the following statements hold.

1) $P_{L\_a(b)(c)}$ when using SHC and DHC are almost equal to each other; this is in line with Fig. 17 where V_L when using them is basically identical.

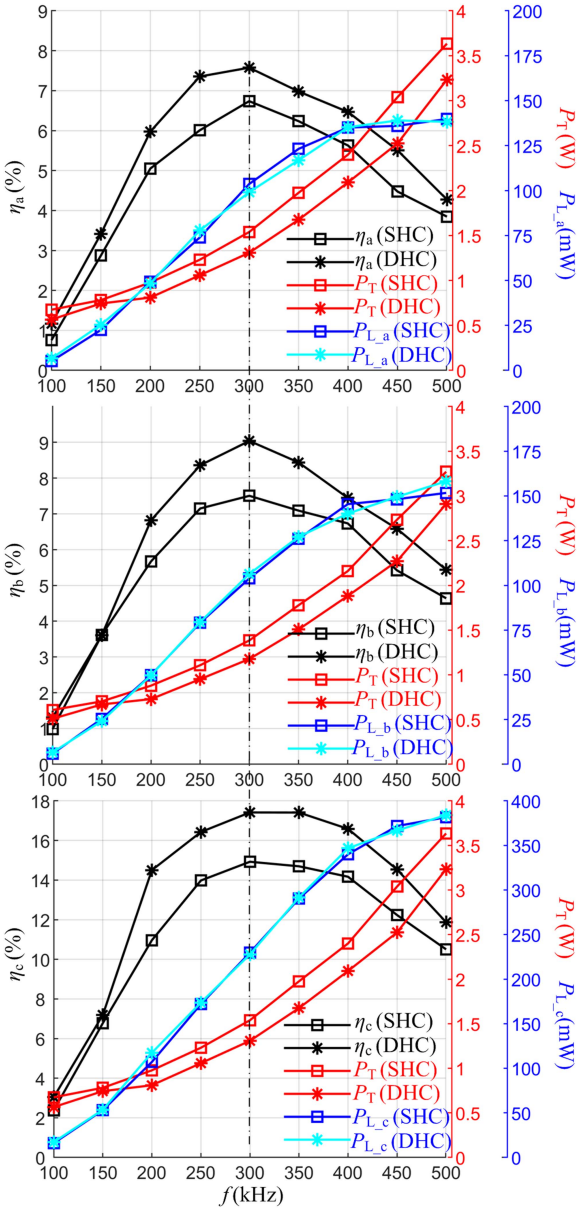

Fig. 18. Changes of $\eta_{a(b)(c)}$, P_T, and $P_{L\_a(b)(c)}$ with f when using SHC and DHC to power a 3DRC.

2) P_T when using DHC is always lower than that when using SHC, enabling DHC to achieve a higher $\eta_{a(b)(c)}$. Note that the difference between P_T when using DHC and SHC is a bit smaller than that in analysis, where the resistance of the tuning components R_{Tun} is assumed to be 0. This is because when generating identical $\mathbf{H_0}$, I_T of DHC is required to be larger than that of SHC, making the tuning components of the DHC consume a higher power.
3) $\eta_{a(b)(c)}$ changes significantly with f; it first increases rapidly with and then decreases rapidly with f, manifesting that an excessive high or low f is indeed not suitable for the application of powering the 3DRC, which has a very small size ($\Phi \leq 15$ mm) and an inserted ferrite core.
4) From the view of maximizing the PTE η, the optimal f for coils a, b, and c is all 300 kHz. At the optimal f, η_a, η_b, and

η_c when using SHC are, respectively, 6.74%, 7.50%, and 14.92%, and they are, respectively, improved to 7.58%, 9.04%, and 17.41% when using DHC.

5) η_b is a bit higher than η_a, and they are all significantly lower than η_c. This is because ε_{rms} of coil b, which can be calculated with the parameters listed in Table III and the formula in [3] is a bit larger than that of coil a, and R_{SR} of coil b is a bit smaller than that of coil a, as listed in Table IV. According to (2), a larger ε_{rms} and a smaller R_{SR} can enable a larger P_L and consequently a higher η. The high η_c is owing to the large E-factor of the ferrite core for coil c. Although coils a, b, and c are all wound around a ferrite core, the equivalent length-diameter ratio of the ferrite core for coil c is the largest, thus enabling a weakest demagnetization effect [24] and a largest E-factor.

A noteworthy issue is that coils a and b have an identical number of turns, and coil b has a larger size and uses more winding wires, but R_{SR} of coil b is smaller than that of coil a. The reason is that the winding wire of coil a at two end faces, is closer to the ferrite core than that of coil b, thus causing a larger copper loss [25].

VI. Discussion

For the 3DRC with design parameters listed in Table III, the optimal f is 300 kHz from the view of maximizing the PTE. Note that the optimal f can change with the 3DRC design parameters. If the coil turns of the 3DRC is reduced, the optimal f may be higher than 300 kHz, because a higher f can compensate ε_{rms} that is lowered by the reduced coil turns. Otherwise, if the coil turns is increased, the optimal f may be lower than 300 kHz.

Although a higher f can reduce the coil turns, i.e., make the 3DRC size more compact, the IWPT system for powering a CR normally uses f less than 500 kHz [3], [4], [5], [6], [9], [10], [11]. The reason is that human safety related to electromagnetic exposure, which is evaluated with an index of specific absorption rate (SAR), must be considered here. SAR can increase rapidly with f, and for the AMF with a higher f, SAR is easier to violate its safety limit, which is 0.4 W/kg for whole-body occupational exposure [26]. In addition, power losses related to inversion, tuning, and rectification, all increase with f. Therefore, f higher than 500 kHz is usually not used in this application, with the consideration of ensuring human safety and improving the PTE.

Besides imposing constraints on f, the human body can increase the parasitic capacitance C_t of DHC/SHC, because it has a much larger dielectric constant than air. The increase in C_t can increase the equivalent resistance R_{ST}, and consequently increase the transmitting power P_T and lower the PTE η, as indicated by (1), (3), and (4). In addition, the increase in C_t can change the reactive component of the DHC/SHC impedance and make the DHC/SHC out of resonance, at this time, the vacuum capacitor and adjustable inductor shown in Fig. 16 should be both reduced for re-resonance. Finally, the increase in C_t can lower the self-resonant frequency of DHC/SHC, which is better to be higher than 1 MHz to ensure the implantation of IWPT operated at 100–500 kHz. To minimize the adverse effect of C_t, the human body should be centered along the central axis of DHC/SHC and avoid any part (e.g., arms and legs) getting close to the winding wire. Note that the human body basically does not change the AMF distribution and the inductance of DHC/SHC, because its relative permeability is basically identical to air.

The parallel connection of ISHC and OSHC enables the DHC to have a smaller R_{ST} than the SHC, and consequently to achieve a higher PTE. It is known to all that by connecting two similar coils in parallel, the dc resistance can be half reduced. However, for the DHC operated at hundreds of kilohertz, its R_{ST} can be lower than that of the SHC only when t_{is} exceeds a certain value. As shown in Fig. 11(b), R_{ST} of DHC ($N = 60$) decreases from 4.32 to 2.01 Ω when t_{is} increases from 2 mm to 80 mm, and it can be lower than that of SHC (3.37 Ω, listed in Table IV) when $t_{is} \geq 11$ mm. This is the reason that the analytical model of the DHC is built to correlate R_{ST} with N and t_{is} in this study, which enables us to select suitable N and t_{is} to improve the PTE. The reason why t_{is} has a significant influence on R_{ST} is explained in Section IV-A.

The comparison between DHC and SHC indicates that a three-layer Helmholtz coil (THC) may be better than DHC. It can be expected that the THC will generate a larger uniform AMF region because its equivalent radius is larger than that of DHC. In addition, when generating identical $\mathbf{H_0}$, the THC will be safer in avoiding peak electromagnetic exposure, because its driving current I_T will be divided into the three layers, and the current in the innermost layer can be smaller than that in the ISHC of DHC. However, the PTE of THC is not necessarily higher than DHC, because R_{ST} of THC maybe just a little smaller than that of DHC, and I_T of THC is larger than that of DHC when generating identical $\mathbf{H_0}$. Note that the difference of R_{ST} between THC and DHC is much smaller than that between DHC and SHC, by analogizing the difference of dc resistance when multiple similar resistances are connected in parallel [27]. C_t of THC is larger than that of DHC, which can further reduce the difference of R_{ST} between them, as indicated by (4). Therefore, DHC may be the best from the view of maximizing the PTE. Certainly, the above conclusion needs further analysis and verification, which will be conducted in our further work.

The PTE to the 3DRC when using the proposed DHC is in a range of 7.58%–17.41%, which is much lower than that of the existing IWPT system for recharging applications [12], [28], but is acceptable for powering the CR. The intention of using the IWPT system here is to solve the challenge of power supply for the CR, which has a very limited size and is targeted to inspect the hard-to-reach human intestine. Assuming the PTE is as low as 5%, the CR power demand is 500 mW, and the inspection process lasts two hours, then we can compute that the required transmitting power is 10 W and the total power consumption is only 0.02 kWh, whose cost is negligible in the expensive endoscopy for the intestine. In fact, the PTE of the IWPT system for CR application is normally less than 10%, as summarized in [3] and [5]. The low PTE is caused by a weak coupling between the DHC/SHC and 3DRC. Because the diameter of DHC/SHC surrounding the human body ($\geq$40 cm) is much larger than that of the 3DRC onboard the CR ($\leq$15 mm); also, the distance between the DHC/SHC and 3DRC is normally larger than 10 cm. The proposed DHC has been proven effective in improving

the PTE compared to the traditional SHC. To further improve the PTE, optimizing the geometry of the ferrite core inserted within the 3DRC to gather more magnetic flux [24], can be a promising way.

VII. Conclusion

A novel DHC for wirelessly powering CR has been presented in this article. The built analytical model of the DHC has been proven correct for calculating the equivalent resistance of the DHC. Based on the analytical model, the optimization flow has been designed, and the optimization results show that the transmitting power of the DHC can be reduced by selecting a suitable insulation layer thickness and large coil turns. The comparison to the SHC has shown the benefits of the DHC in generating a uniform AMF to cover a larger region, lowering peak electromagnetic exposure near the winding wire, and reducing the transmitting power when generating identical AMF. The DHC with optimized design parameters has been used to power the 3DRC, and the achieved PTE was higher than that when using the SHC, manifesting it is promising to construct a more efficient platform-type IWPT system for powering the CR.

References

[1] J. Gao, Z. Zhang, and G. Yan, "Locomotion analysis of a clamper-based capsule robot in a compliant tube," *IEEE/ASME Trans. Mechatronics*, vol. 26, no. 1, pp. 55–65, Feb. 2021.

[2] S. Song et al., "Integrated design and decoupled control of anchoring and drug release for wireless capsule robots," *IEEE/ASME Trans. Mechatronics*, vol. 27, no. 5, pp. 2897–2907, Oct. 2022.

[3] J. Gao et al., "Stable wireless power transmission for a capsule robot with randomly changing attitude," *IEEE Trans. Power Electron.*, vol. 38, no. 2, pp. 2782–2796, Feb. 2023.

[4] H. Zhuang, W. Wang, and G. Yan, "Omnidirectional wireless power transfer system using modified saddle-shaped coil pair for implantable capsule robots," *IEEE Trans. Power Electron.*, vol. 38, no. 9, pp. 11664–11672, Sep. 2023, doi: 10.1109/TPEL.2023.3270501.

[5] M. R. Baser, M. Y. Ahmad, J. Cho, and F. Ibrahim, "Application of wireless power transmission systems in wireless capsule endoscopy: An overview," *Sensors*, vol. 14, no. 6, pp. 10929–10951, 2014.

[6] S. Roy, A. N. M. W. Azad, S. Baidya, M. K. Alam, and F. Khan, "Powering solutions for biomedical sensors and implants inside the human body: A comprehensive review on energy harvesting units, energy storage, and wireless power transfer techniques," *IEEE Trans. Power Electron.*, vol. 37, no. 10, pp. 12237–12263, Oct. 2022.

[7] H. Liu, Q. Shao, and X. Fang, "Modeling and optimization of class-E amplifier at subnominal condition in a wireless power transfer system for biomedical implants," *IEEE Trans. Biomed. Circuits Syst.*, vol. 11, no. 1, pp. 35–43, Feb. 2017.

[8] D. Kim and D. Ahn, "Self-tuning LCC inverter using PWM-controlled switched capacitor for inductive wireless power transfer," *IEEE Trans. Ind. Electron.*, vol. 66, no. 5, pp. 3983–3992, May 2019.

[9] Q. Ke, W. Luo, G. Yan, and K. Yang, "Analytical model and optimized design of power transmitting coil for inductively coupled endoscope robot," *IEEE Trans. Biomed. Eng.*, vol. 63, no. 4, pp. 694–706, Apr. 2016.

[10] M. R. Baser, M. Y. Ahmad, J. Cho, and F. Ibrahim, "Stable and high-efficiency wireless power transfer system for robotic capsule using a modified Helmholtz coil," *IEEE Trans. Ind. Electron.*, vol. 64, no. 2, pp. 1113–1122, Feb. 2017.

[11] M. R. Baser, M. Y. Ahmad, J. Cho, and F. Ibrahim, "An improved wearable resonant wireless power transfer system for biomedical capsule endoscope," *IEEE Trans. Ind. Electron.*, vol. 65, no. 10, pp. 7772–7781, Oct. 2018.

[12] N. Ha-Van, Y. Liu, P. Jayathurathnage, C. R. Simovski, and S. A. Tretyakov, "Cylindrical transmitting coil for two-dimensional omnidirectional wireless power transfer," *IEEE Trans. Ind. Electron.*, vol. 69, no. 10, pp. 10045–10054, Oct. 2022.

[13] J. Gao and G. Yan, "Design and implementation of a clamper-based and motor-driven capsule robot powered by wireless power transmission," *IEEE Access*, vol. 7, pp. 138151–138161, 2019.

[14] S. R. Khan, S. K. Pavuluri, G. Cummins, and M. P. Y. Desmulliez, "Miniaturized 3-D cross-type receiver for wirelessly powered capsule endoscopy," *IEEE Trans. Microw. Theory Techn.*, vol. 67, no. 5, pp. 1985–1993, May 2019.

[15] J. Gao et al., "Design and testing of a motor-based capsule robot powered by wireless power transmission," *IEEE/ASME Trans. Mechatronics*, vol. 21, no. 2, pp. 683–693, Apr. 2016.

[16] Z. Miao, D. Liu, and C. Gong, "Efficiency enhancement for an inductive wireless power transfer system by optimizing the impedance matching networks," *IEEE Trans. Biomed. Circuits Syst.*, vol. 11, no. 5, pp. 1160–1170, Oct. 2017.

[17] J. Gao and G. Yan, "A novel power management circuit using a supercapacitor array for wireless powered capsule robot," *IEEE/ASME Trans. Mechatronics*, vol. 22, no. 3, pp. 1444–1454, Jun. 2017.

[18] G. Zhou, "The equivalent self-inductance of N coupled parallel coils," *Prog. Electromagn. Res. Lett.*, vol. 46, pp. 59–66, May 2014.

[19] A. K. RamRakhyani, S. Mirabbasi, and M. Chiao, "Design and optimization of resonance-based efficient wireless power delivery systems for biomedical implants," *IEEE Trans. Biomed. Circuits Syst.*, vol. 5, no. 1, pp. 48–63, Feb. 2011.

[20] Z. Yang, W. Liu, and E. Basham, "Inductor modeling in wireless links for implantable electronics," *IEEE Trans. Magn.*, vol. 43, no. 10, pp. 3851–3860, Oct. 2007.

[21] J. A. Ferreira, "Improved analytical modeling of conductive losses in magnetic components," *IEEE Trans. Power Electron.*, vol. 9, no. 1, pp. 127–131, Jan. 1994.

[22] M. Wu et al., "Modeling of litz-wire DD coil with ferrite core for wireless power transfer system," *IEEE Trans. Power Electron.*, vol. 38, no. 5, pp. 6653–6669, May 2023.

[23] J. Gao et al., "Analysis of connection way of a three-dimensional receiving coil onboard a capsule robot for wireless power transmission," *Prog. Electromagn. Res. M*, vol. 78, pp. 39–48, Jan. 2019.

[24] M. Wang, J. Feng, Y. Shi, and M. Shen, "Demagnetization weakening and magnetic field concentration with ferrite core characterization for efficient wireless power transfer," *IEEE Trans. Ind. Electron.*, vol. 66, no. 3, pp. 1842–1851, Mar. 2019.

[25] M. Spang and M. Albach, "Optimized winding layout for minimized proximity losses in coils with rod cores," *IEEE Trans. Magn.*, vol. 44, no. 7, pp. 1815–1821, Jul. 2008.

[26] International Commission on Non-Ionizing Radiation Protection (ICNIRP) et al., "Guidelines for limiting exposure to electromagnetic fields (100 kHz to 300 GHz)," *Health Phys.*, vol. 118, no. 5, pp. 483–524, 2020.

[27] A. Roßkopf, E. Bar, and C. Joffe, "Influence of inner skin- and proximity effects on conduction in Litz wires," *IEEE Trans. Power Electron.*, vol. 29, no. 10, pp. 5454–5461, Oct. 2014.

[28] Y. Yao, P. Sun, X. Liu, Y. Wang, and D. Xu, "Simultaneous wireless power and data transfer: A comprehensive review," *IEEE Trans. Power Electron.*, vol. 37, no. 3, pp. 3650–3667, Mar. 2022.

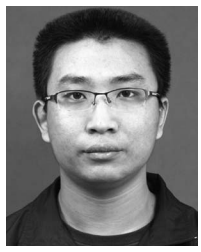

Jinyang Gao was born in Shanxi, China, in 1990. He received the B.S. degree from the University of Electronic Science and Technology of China, Sichuan, China, in 2012, and the Ph.D. degree from Shanghai Jiaotong University, Shanghai, China, in 2017, both in instrument science and technology.

He joined the North University of China, Shanxi, China, in 2017, where he became an Associate Professor in 2019. Since 2021, he has been an honorary Research Associate with the Department of Mechanical and Automation Engineering, The Chinese University of Hong Kong, Hong Kong. He authored 15 peer-reviewed papers as the first author and 12 Chinese invention patents. His research interests include capsule robots, wireless power transmission and related electronic circuit design, and gastrointestinal biomechanics.

Dr. Gao is the recipient of the National Excellent Doctoral Dissertation of China in the field of measurement and control technology and instrument in 2018.

Siyu Tian was born in Shanxi, China, in 1999. She received the B.S. degree in instrument science and technology in 2021 from the North University of China, Shanxi, China, where she is currently working toward the M.S. degree in instrument science and technology.

Her research interests include magnetic tracking and capsule robots.

Changshun Yuan was born in Shanxi, China, in 1987. He received the B.S. and Ph.D. degrees in electronic engineering from Beihang University, Beijing, China, in 2010 and 2016, respectively.

From 2017 to 2018, he was an Engineer with Huawei Technology Co., Ltd. He is currently an Associate Researcher with Hangzhou Innovation Institute, Beihang University, Hangzhou, China.

Ziyu Ma was born in Shanxi, China, in 2000. He received the B.S. degree in electronic engineering in 2022 from the North University of China, Shanxi, China, where he is currently working toward the M.S. degree in instrumentation engineering.

His research interests include capsule robots and wireless power transmission.

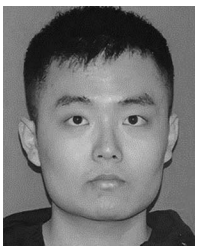

Chen Gao was born in Shanxi, China, in 1995. He received the B.S. degree in electronic engineering in 2018 from the North University of China, Shanxi, China, where he is currently working toward the M.S. degree in electronic engineering.

His research interests include capsule robots and wireless power transmission.

Guozheng Yan was born in Hunan, China, in 1961. He received the Ph.D. degree in mechanical engineering from the Jilin University of Technology, Jilin, China, in 1993.

In 1995, he became a Postdoctoral Fellow with the Nanjing University of Aeronautics and Astronautics, Jiangsu, China. In 1997, he became a Professor with the Department of Instrument Science and Engineering, Shanghai Jiaotong University, Shanghai, China. His research interests include biomedical electronics, microsensors, microelectromechanical systems, and instrument engineering.

Ruiqin Li was born in Shanxi, China, in 1964. She received the B.S. degree in mechanical manufacturing technology and equipment from the Beijing Institute of Technology, Beijing, China, in 1985, and the Ph.D. degree in mechanical design and theory from Shanghai Jiaotong University, Shanghai, China, in 2004.

Since 2005, she has been a Professor with the North University of China, Shanxi, China. Her research interests include mechanism configuration innovation, bionic mobile robots, and exoskeleton rehabilitation robots.

Dr. Li was the recipient of the Natural Science Award of Shanxi Province, China, in the field of type synthesis of parallel mechanisms in 2021.

Qiulin Tan (Senior Member, IEEE) received the B.S. degree in mechanical engineering, the M.S., and Ph.D. degrees in instrument science and technology from the North University of China, Shanxi, China, in 2002, 2006, and 2009, respectively.

He held a postdoctoral position with Tsinghua University in 2015. He is currently a Professor with the North University of China. His current research interests include nanomaterials, IR gas sensors, wireless passive microsensors, smart flexible sensors, wireless power transfer, and surface acoustic wave sensors.

Li Zhang (Fellow, IEEE) received the Ph.D. degree in physics from the University of Basel, Basel, Switzerland, in 2007.

He was a Postdoctoral Fellow and a Senior Scientist with the Institute of Robotics and Intelligent Systems, Swiss Federal Institute of Technology (ETH), Zurich, Switzerland. He is currently a Professor with the Department of Mechanical and Automation Engineering, The Chinese University of Hong Kong, Hong Kong. His research interests include small-scale robotics for biomedical applications and their collective behaviors for the development of intelligent robot swarms.